NANOSCALE STRUCTURE/PROPERTY CORRELATION THROUGH ABERRATION-CORRECTED STEM AND THEORY

S. J. PENNYCOOK[1,2], A. R. LUPINI[1], M. VARELA[1], A. BORISEVICH[1], M. F. CHISHOLM[1], E. ABE[1,3], N. DELLBY[4], O. L. KRIVANEK[4], P. D. NELLIST[4], L. G. WANG[1#], R. BUCZKO[1,2,5], X. FAN[1*], and S. T. PANTELIDES[1,2],

[1]Condensed Matter Sciences Division, Oak Ridge National Laboratory, Oak Ridge, TN

[2]Department of Physics and Astronomy, Vanderbilt University, Nashville, TN

[3]National Institute for Materials Science, 1-2-1 Sengen, Tsukuba, Japan

[4]Nion Co., 1102 8th Street, Kirkland, WA

[5]Institute of Physics, Polish Academy of Sciences, 02-668 Warsaw, Poland

[#]Now at National Renewable Energy Laboratory, Golden, CO

[*]Now at Center for Advanced Microscopy, Michigan State University, East Lansing, MI

INTRODUCTION

The combination of atomic-resolution Z-contrast microscopy, electron energy loss spectroscopy and first-principles theory has proved to be a powerful means for structure property correlations at interfaces and nanostructures[1,2,3,4]. The scanning transmission electron microscope (STEM) now routinely provides atomic-sized electron beams[5], allowing simultaneous Z-contrast imaging and EELS as shown in Fig. 1. The feasiblity of correcting the inherently large spherical aberration of microscope objective lenses promises to at least double the achievable resolution[6,7]. The potential benefits for the STEM, however, may turn out to be much greater than those for the conventional TEM because it is very much less sensitive to chromatic instabilities[8]. The 100 kV VG Microscopes HB501UX at Oak Ridge National Laboratory (ORNL) is now fitted with an aberration corrector constructed by Nion Co., which improved its resolution from 2.2 Å (full-width-half-maximum probe intensity) to around 1.3 Å. It is now very comparable in performance to the *uncorrected* 300 kV HB603U STEM at ORNL which, before correction, also had a directly interpretable resolution of 1.3 Å, although information transfer had been demonstrated down to 0.78 Å[8]. Initial results after installing an aberration corrector on the 300 kV STEM indicate a resolution of 0.84 Å. The theoretically achievable probe size in the absence of instabilities is predicted to be 0.5 Å.

The Z-contrast image[9,10,11] is a very convenient and intuitive method for revealing atomic arrangements, even if those configurations are unexpected. Examples include isolated dislocation cores[12] and also dislocation arrays that comprise grain boundaries.[13, 14] The STEM appears to be the only viable means for obtaining spectroscopic analysis at atomic resolution. Locating the probe on an individual atomic column selected from the image allows EELS measurements of local elemental concentrations and electronic structure.[15,16]

These techniques are ideally complementary to first-principles total-energy calculations. The structures suggested from experiment avoid the need to search the large number of possible defect configurations. Theory can efficiently perform structural relaxations of configurations suggested from experiment, to confirm and refine the suggested structure. Theory can also provide segregation energies for impurities and point defects and the local electronic structure and optical properties.[17,18] Only with theory can the real functionality of interfaces and

nanostructures be determined, as we show in two examples below. The first example shows how CdSe nanocrystals act as catalysts for the fixation of CO_2, while the second shows the nucleation pathway for single wall carbon nanotubes applicable to conditions of laser-ablation growth.

Calculations were performed using density functional theory[19], the generalized-gradient approximation for the exchange-correlation potential[20], Vanderbilt ultrasoft pseudopotentials,[21] with a plane-wave energy cutoff of 350 eV as determined by convergence studies. For CdSe nanocrystals we considered the $(10\bar{1}0)$, (0001), $(000\bar{1})$ and $(10\bar{1}2)$ surfaces[22], using a 2x2 supercell with six atomic layers separated by a vacuum layer of 14 Å, and 2 special k-points in the irreducible wedge of the Brillouin zone in conjunction with the Monkorst-Pack scheme[23]. The surface atomic arrangements and the configuration of the adsorbed CO_2 molecule were optimized until the forces on atoms were smaller than 0.05 eV/ Å. The convergence of the results was checked with respect to supercell size, the slab and vacuum thickness, and k-points. For the nanotube nucleation calculations, an energy cutoff of 380 eV was used. Various carbon clusters were placed on a Ni (100) surface and relaxed. Several initial locations were used to find the lowest energy position for each cluster.

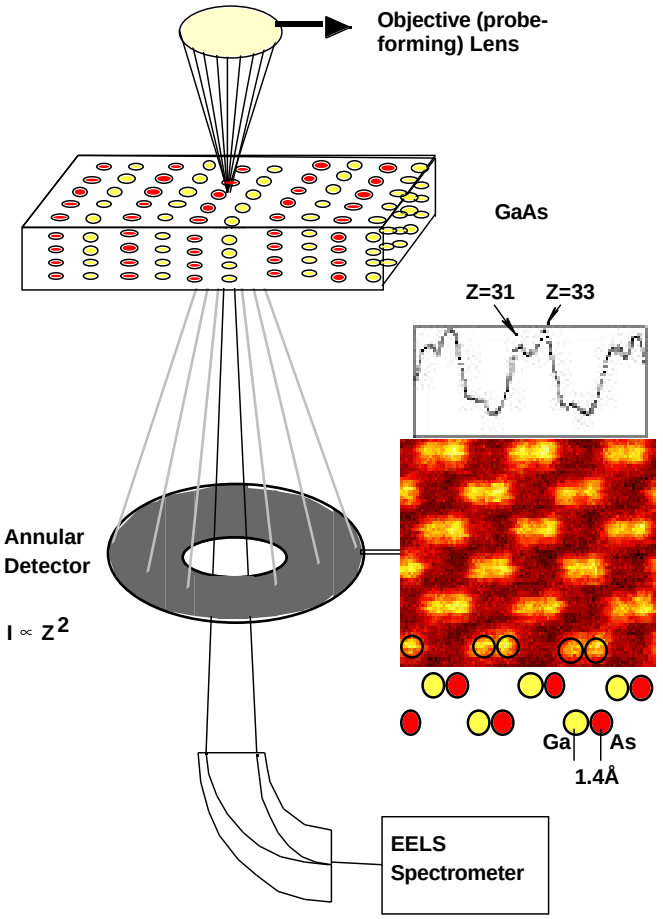

Fig. 1. Schematic showing simultaneous Z-contrast imaging and EELS in the STEM. The image distinguishes the sublattice polarity in GaAs.

PERFORMANCE OF THE ORNL 100 kV ABERRATION CORRECTED STEM

The correction of objective lens aberration is achieved though a set of multipole lenses that produce negative spherical aberration (C_s) to cancel the inherent large positive C_s of the conventional round objective lens. Computer diagnosis and correction of aberrations then enables the probe-forming aperture to be enlarged to produce a smaller probe, as shown in Fig. 2.

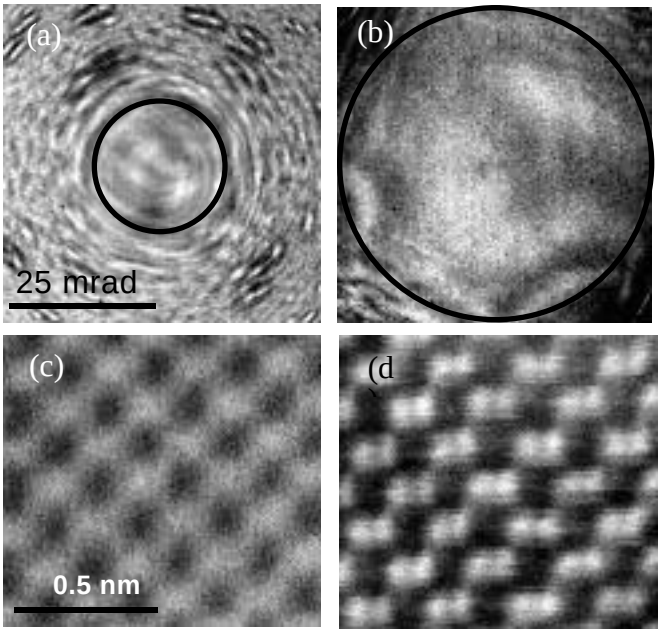

Fig. 2. Ronchigram observed in far-field with a probe stationary on the sample showing the extent of uniform phase (a) for the uncorrected microscope (b) after aberration correction. Images of Si 110 show the improvement in image resolution from (c) 2.2 Å to (d) 1.3 Å which now resolves the dumbbells.

Figure 3 shows the sensitivity to single atoms available at 100 kV with the enhanced resolution, where single Bi atoms on lattice sites within the crystal are visible. Similar results have been shown also for Sb atoms in Si using an uncorrected 200 kV microscope[24]. In our case, intensity profiles across the image reveal which of the two columns of the dumbbell contain the Bi atom. The density of bright spots correlates with the known dose of Bi, which was introduced by ion implantation followed by recrystallization through solid phase epitaxial growth. The sample was prepared by standard ion milling procedures using a final cleaning at 0.5 kV.

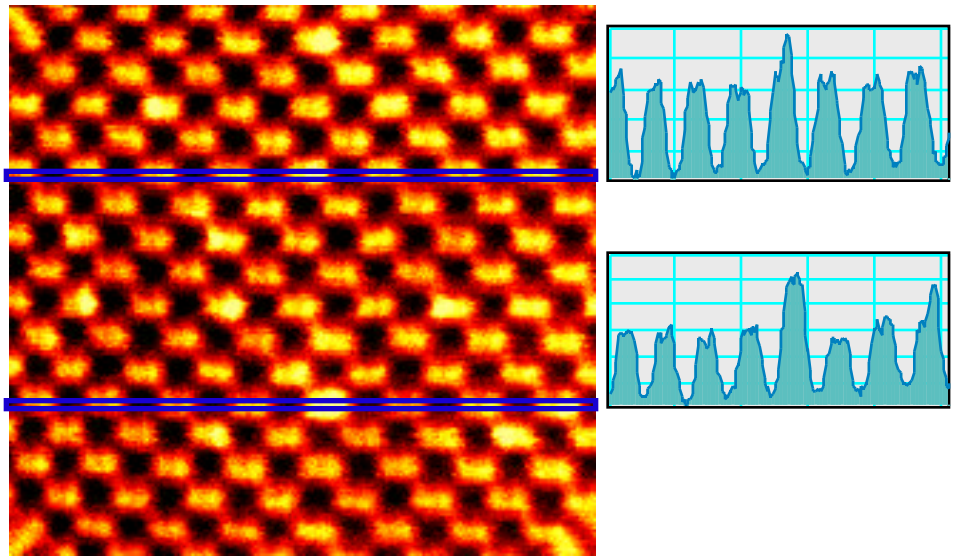

Fig. 3. Z-contrast image of Bi-doped Si 110 revealing the columns containing individual Bi atoms. The upper intensity profile shows a Bi atom on the right hand column of a Si dumbbell, the lower profile shows a Bi atom in each of the two columns of a dumbbell.

The thickness on this region was estimated at 300 Å, close to one extinction distance of the 1s Bloch state which is responsible for the image contrast[9-11]. In this case, a single atom will show depth dependent contrast due to the periodic nature of the dynamical wave field. A channeling model provides an approximate analytical description of the process, and Fig 4(a) shows the oscillation of detected intensity as a function of depth in the crystal. The total signal generated in a Si sample of a given thickness is then the integral of this curve, shown in Fig. 4(b), which saturates when all the 1s state has been scattered onto the detector. The intensity of Bi atoms in a sample just one-half extinction distance in thickness is therefore a direct indication of its depth. In practice, the extinction is not complete due to the differing phases of the other Bloch states, and the oscillations occur on a slowly rising background. More accurate image simulations are needed to take account of such effects, but the simple channeling model nicely illustrates the underlying physics.

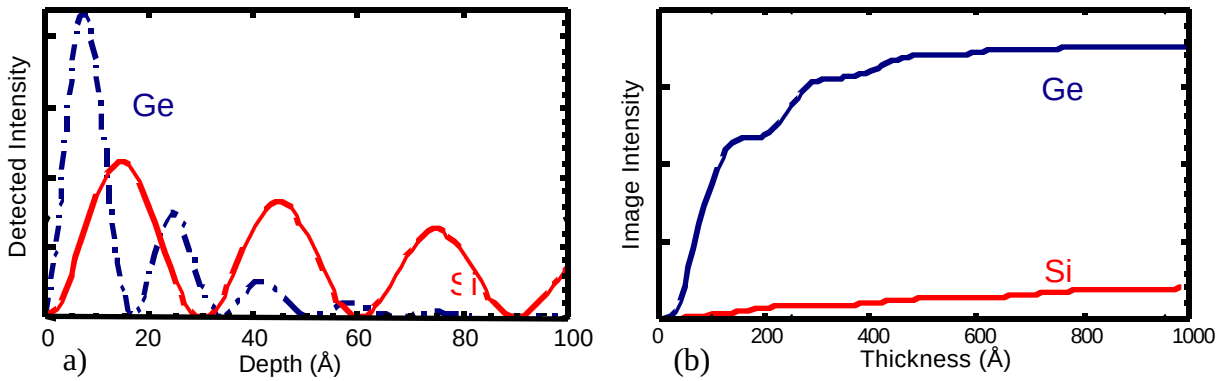

Fig. 4. (a) Generation of detected intensity in Si and Ge as a function of depth in the crystal, calculated with a channeling model showing the extinction oscillations. (b) The image intensity is the thickness integral of (a). Single substitutional Bi atoms will sample the oscillating wave field in (a) and show a depth dependent image contrast, as observed experimentally.

An ideal demonstration of the ability of the STEM to probe highly localized changes in electronic structure is provided by the high T_c superconductor YBCO. In this layered structure, superconductivity is believed to occur as a result of charge transfer from the CuO chain plane, where the Cu valence is nominally +1, to the CuO_2 plane where the Cu valence is nominally +2. The Cu $L_{2,3}$ white line ratio should therefore change on moving the probe from the chains to the planes, a distance of only ~ 4 Å. As seen in Fig 5, this is exactly what is observed experimentally. Furthermore, it has been well-established that a pre-peak observed on the O K edge is directly related to the density of holes responsible for superconductivity. Fig. 5 also shows that this pre-peak appears present in the planes but not in the chains, suggesting hole localization in the CuO_2 planes. Further studies are required to ensure that damage effects are not playing a role, but this is an excellent demonstration of the local nature of the information in the EELS spectrum. Because of dynamical scattering, the probe explores neighboring columns as it propagates through the specimen, but the information seen by a large angle EELS detector is still highly localized, almost as highly localized as with the high angle annular dark field detector itself.[25]

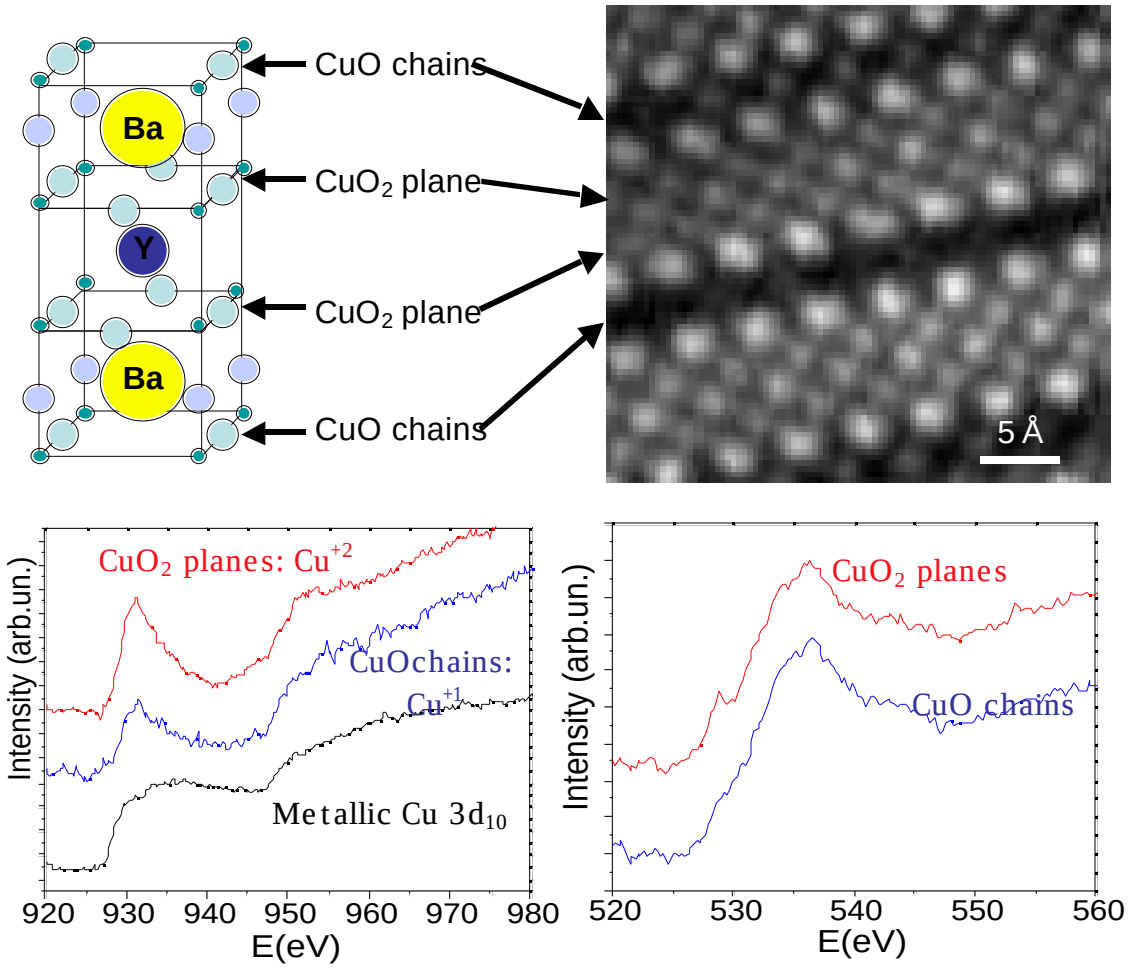

Fig. 5. Schematic of YBCO structure with Cu/O planes and chains arrowed in the Z-contrast image. Spectra obtained from the chains and planes separately show (left) their different $L_{2,3}$ ratio at the Cu edge, with metallic Cu as a reference, and (right) a prepeak in the O K edge region of the spectra indicating holes localized in the planes.

Figure 6 shows an image of small CdSe/ZnS core/shell nanocrystals synthesized by Quantum Dot Corporation using standard methods[26]. In the raw Z-STEM image it is easy to distinguish the core from the shell just on the basis of image intensity: the core is seen as a bright yellow/white region in the center and the shell is seen as a yellow/red region around it. Quality and coverage of the shell and location of the core relative to the shell, two properties which might influence the fluorescence quantum efficiency, can easily be determined using Z-STEM. The single atom visible in the circle shows the greatly improved sensitivity of the aberration-corrected STEM. Addition of a cathodoluminescence detector would enable the effectiveness of the passivating shell to be determined nanocrystal by nanocrystal.

Fig. 6. Z-contrast image of CdSe/ZnS core/shell nanocrystals. The core is seen as a bright yellow/white region in the center and the shell is seen as a surrounding yellow/red region.

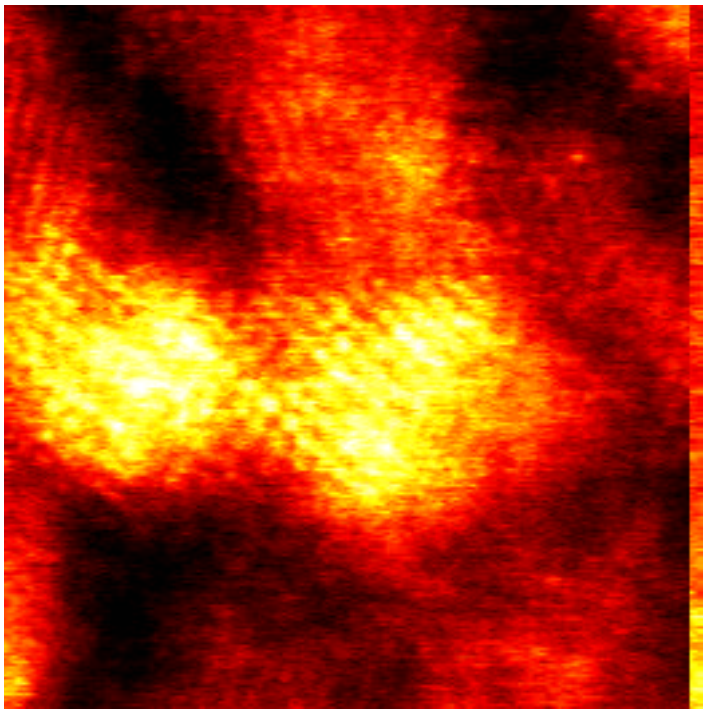

Because the Z-contrast image is an incoherent image, in thin crystals the intensity is directly related to the number of atoms in the column as well as their atomic number. For nanocrystals of a single composition with well defined facets it is possible to invert the intensities to extract the three-dimensional shape of individual nanocrystals[27]. At present the accuracy of such a reconstruction is limited by the signal to noise ratio in the image, but as probe sizes continue to be reduced, and the signal to noise ratio improves, accurate reconstruction of shapes and exposed facets will become possible. Such information is important for understanding the functionality of nanocrystals, especially in areas such as catalysis.

INITIAL RESULTS FROM THE ORNL 300 KV ABERRATION-CORRECTED STEM

Figure 7 compares the performance before and after fitting a Nion aberration-corrector to the ORNL 300 kV STEM. On the left is the Scherzer optimum probe profile for the uncorrected microscope, the Ronchigram, and an image and line trace from Si 110 . The right hand side shows the 0.5 Å probe predicted after aberration-correction, showing the same current squeezed into a smaller, brighter probe. Such a probe should therefore give greatly improved contrast and signal to noise ratio from single atoms and crystals with spacings in the 1 – 2 Å range. Experimentally, the Ronchigram does show the anticipated 2.5-fold increase in the extent of flat phase, indicating that an instantaneous probe of 0.5 Å size has indeed been generated by the corrector. The resolution obtained in the image, however, is limited to around 0.9 Å due to instabilities. Nevertheless, the Si 110 image now shows more contrast, with much deeper dips between the dumbbells. In addition, the effect of probe tails has been much reduced. We no longer see the weak subsidiary maxima in the center of the channels that are present in the uncorrected image. These features come from the extended tails on the uncorrected probe. When this probe is centered on a channel, the tail overlaps the nearest six columns of Si giving a weak

secondary peak. After correction the tails are reduced in intensity and brought closer to the central peak so this spurious feature is no longer present.

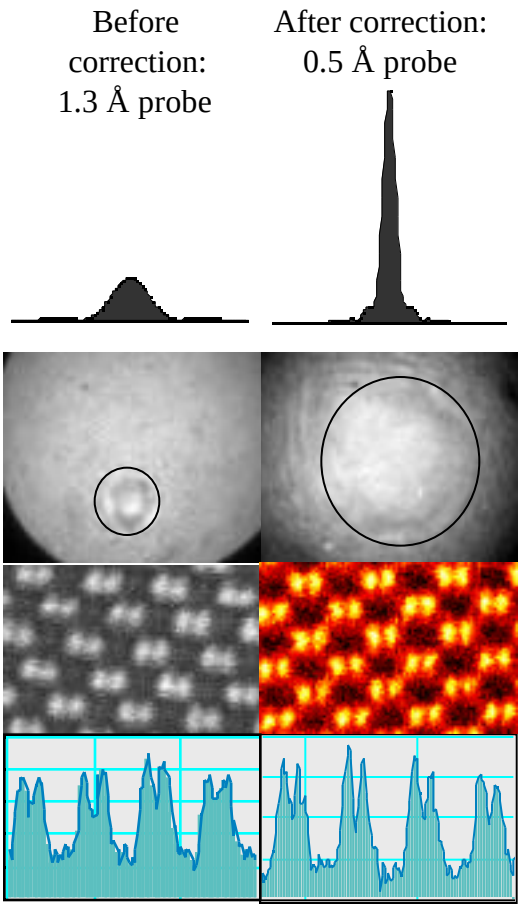

Fig. 7. Comparison of the performance of the 300 kV STEM before correction (left) and after installation of the aberration corrector (right). Panels show, from top to bottom, the theoretical probe profile, experimental Ronchigrams and images and intensity profiles of Si 110 .

The present resolution limit achieved in a crystal of SiC in the $1\bar{1}00$ orientation is 0.84 Å, as shown in Fig. 8 below.

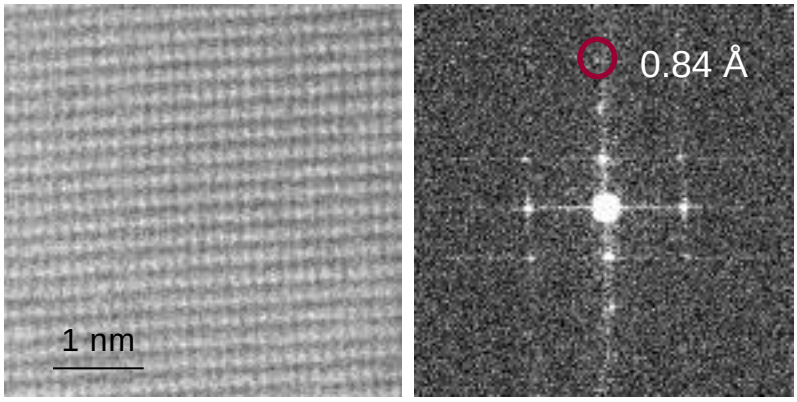

Fig. 8. Image of 4H SiC in the $1\bar{1}00$ orientation (left) and its Fourier transform (right) showing the presence of the (0 0 12) spacing at 0.84 Å.

Another measure of resolution is available from images of single atoms. Figure 9 compares images of single La atoms on a γ-alumina support before (a) and after (b, c) aberration correction. Although they are visible in both images, they show more contrast and a better signal to noise ratio after correction. A histogram of the full-width-half-maxima (FWHM) of intensity profiles across single La atoms (Fig. 9 (b), inset) gives the probe FWHM as about 0.7 – 0.8 Å. Line scans were taken in the vertical direction to avoid the effects of drift, which was predominantly in the horizontal direction. The smaller probe also gives a greatly improved image from the alumina itself. Although very faint lattice fringes can be discerned in the uncorrected image (arrowed), after correction, individual Al/O columns are clearly seen in Fig. 9 (c). The La atom positions are directly seen to coincide with (100) atomic columns of the spinel lattice of γ-Al_2O_3.

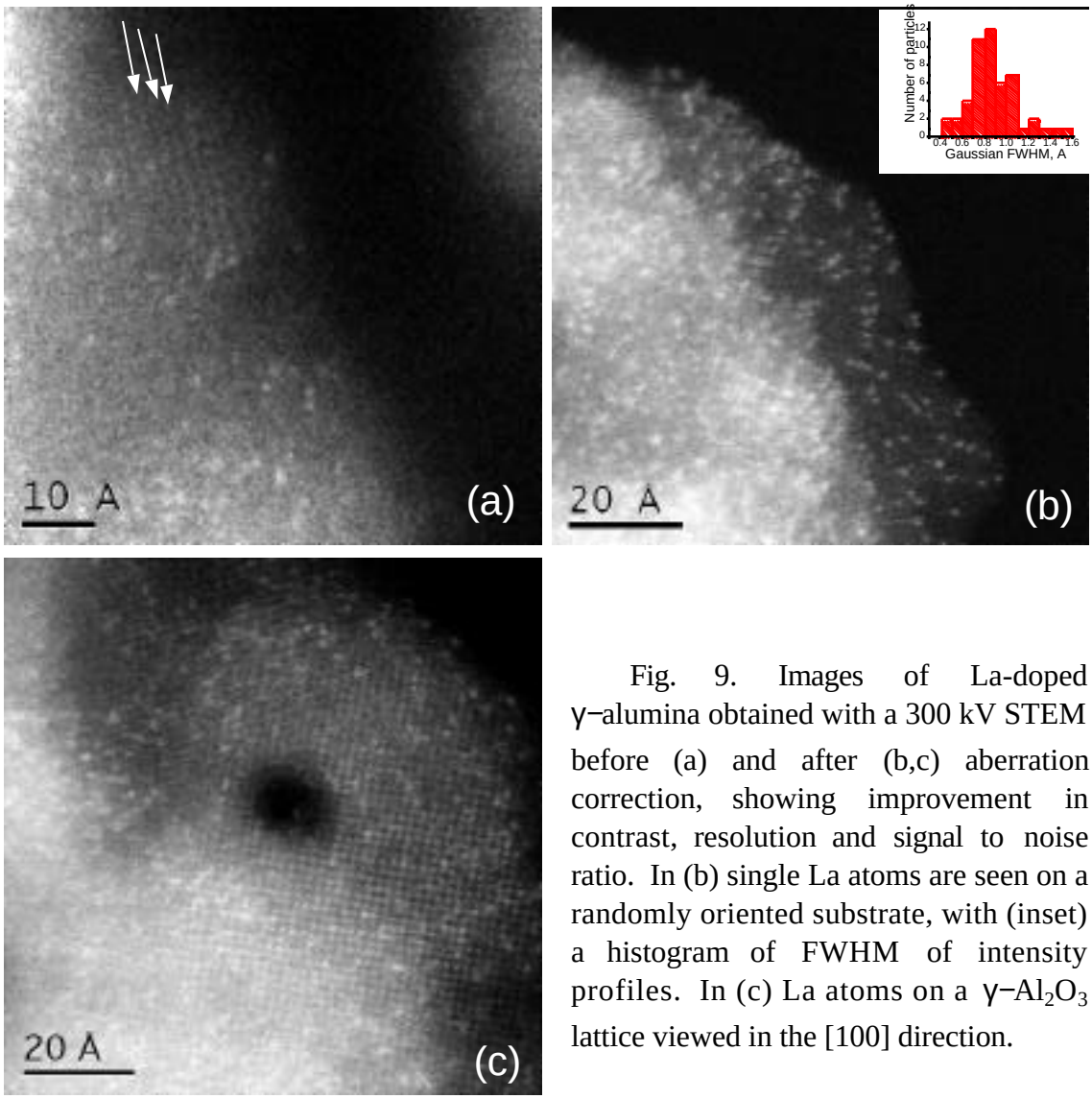

Fig. 9. Images of La-doped γ−alumina obtained with a 300 kV STEM before (a) and after (b,c) aberration correction, showing improvement in contrast, resolution and signal to noise ratio. In (b) single La atoms are seen on a randomly oriented substrate, with (inset) a histogram of FWHM of intensity profiles. In (c) La atoms on a γ−Al_2O_3 lattice viewed in the [100] direction.

THEORETICAL INVESTIGATION OF NANOSTRUCTURE FUNCTIONALITY AND NUCLEATION

Cd-rich CdSe nanocrystals below a certain critical size are efficient photo-catalysts for the fixation of CO_2, however, CdSe surfaces are not. In contrast, bulk CdS and ZnS surfaces do catalyze in the presence of light. First-principles calculations show that on flat stoichiometric CdSe surfaces a CO_2 molecule physisorbs and is no more reactive than in the free state. At a Cd vacancy, however, strong chemisorption occurs, and the molecule draws extra electron density from the back bonds to become negatively charged. The barrier for desorption is ~0.3 eV suggesting that, even at room temperature, CO_2 molecules would be constantly chemisorbing and desorbing. If a chemisorbed molecule could desorb and carry an extra electron with it, it would be highly reactive. The energy cost is high, however, (1.3 eV, see Fig. 10a). Photoexcitation, which excites electrons to the conduction bands is essential for the catalytic process to occur. Doping

the crystal n-type in the calculation reduces the energy cost to only 0.4 eV (Fig. 10c). It is now that a nanocrystal enters the scene as an absolute necessity. The energy gap of a nanocrystal increases with decreasing size. The critical diameter to enable the free flow of crystal electrons to desorbing CO_2 molecules is estimated at about 3.5 nm, which compares well with the experimental value of 5 nm. CdS and ZnS have larger bandgaps so that nanocrystals are not required.

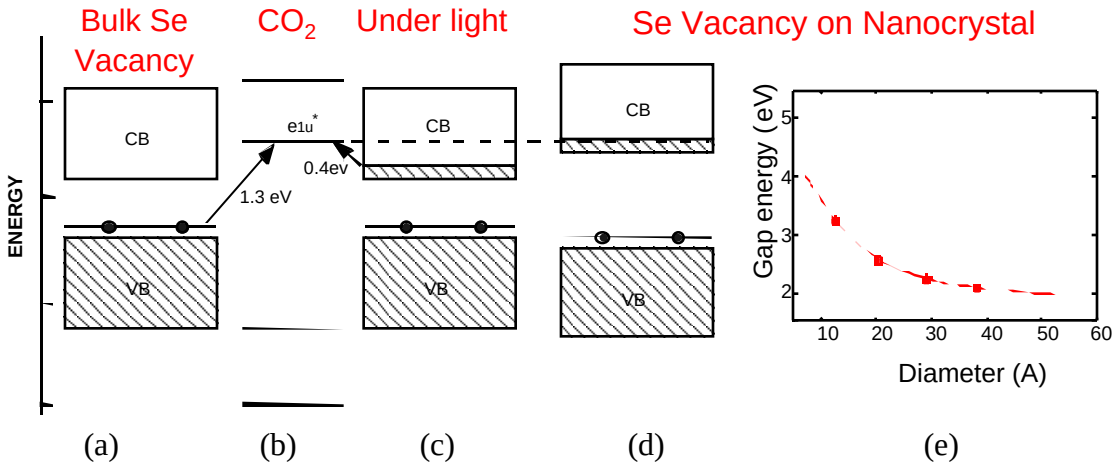

Fig. 10. Schematic showing the calculated relative energy levels of the conduction band (CB) and valence band (VB) at a Se vacancy in bulk CdSe (a) relative to the (b). Photoexcitation puts an electron in the conduction band, reducing the energy required to promote it to the antibonding CO_2 orbital from 1.3 to 0.4 eV. The additional 0.4 eV can be provided by a Se vacancy on a Nanocrystal (c), due to the increase in band gap with decreasing nanocrystal size.[28]

The calculations show first, that catalysis can occur away from a surface by generation of mobile reactive species, second, that the most important role of the nanoscale is the opening of the band gap and third, that doping may avoid the need to provide light for the reaction to occur[29]. Such understanding may assist effective implementation of semiconductor nanocrystals to alleviate global warming and the depletion of fossil fuels.

Another process that is accessible via theory but very difficult to probe experimentally is that of nucleation. As an example, we consider the case of the nucleation of single wall carbon nanotubes during laser ablation. Z-contrast images show the metal catalyst particles clearly, and through EELS composition profiles can be obtained even across the smallest particles present (~ 2 nm diameter)[30]. However, it would be impossible to see the nucleation of the first few carbon atoms into a nanotube. *After* nucleation, growth may be observable via in-situ microscopy, but the initial stages are completely inaccessible to direct observation because of the high temperatures, the short time scales of nucleation, and the need to see individual carbon atoms on the surface of molten metal. Theory, however, can probe various possible configurations of carbon atoms on a metal, and can demonstrate a viable nucleation pathway. In laser ablation growth, both the carbon and catalyst atoms condense from the gas phase into metal/carbon liquid drops. As they cool through the eutectic point, carbon will be rejected from the metal and nucleates on the surface. With first-principles theory we have examined various possible forms of carbon nuclei, with increasing size, so as to elucidate the general form of nucleation pathway.

We stress we do not need to follow each atom's motion, as the process is statistical in nature, but just determine the lowest energy form of nucleus as a function of the number of carbon atoms. The results are shown in Fig. 11, and show that it is energetically favorable to introduce pentagons at the earliest stages of nucleation. Although pentagons introduce curvature and have an associated energy cost, they allow the dangling bonds around the periphery of the flake to saturate in the metal surface. The lowest energy structure on a metal surface is a hemispherical cap or capped tube. Subsequently the structure can grow by a root growth mechanism.

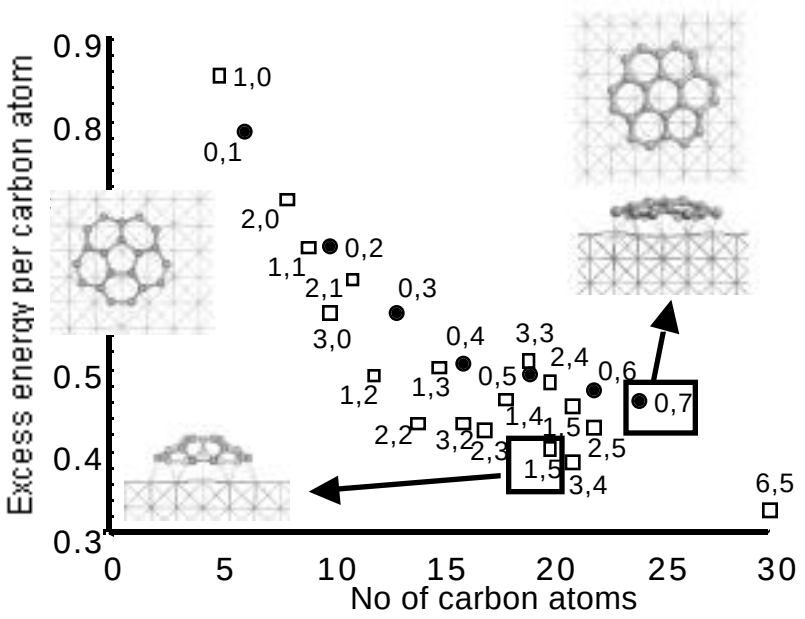

Fig. 11. Determination of the nucleation pathway for single wall carbon nanotubes during laser ablation growth. First-principles calculations show the excess energy per carbon atom relative to a graphite for various clusters on a Ni surface. Structures containg hexagons are shown as solid points, structures containing pentagons as squares. Points are labeled according to the number of (pentagons, hexagons) in each structure. It is clear that pentagons are incorporated at the earliest stages in order to facilitate curvature, and reduce the energy associated with dangling bonds at the perimeter.

SUMMARY

Aberration correction is enabling smaller, brighter probes to be realized with enormous improvements not only in resolution but also in image contrast and signal to noise ratio. Microscopy will no longer be limited by the instrument but by the sample. In a zone axis crystal, the image resolution will be limited by dynamical diffraction. The fundamental quantum mechanical limit to resolution is set by the 1s Bloch states, which are typically ~ 0.5 Å in width. The Z-contrast image will be a direct image of the 1s Bloch states.[31] Spectacular improvement will also be seen for EELS. Increasing the current down one selected column, and simultaneously decreasing the current illuminating surrounding columns, will improve the analytical sensitivity dramatically. Single impurity atom detection should be possible in specific columns at a grain boundary or dislocation core, and at specific sites on a crystal surface. Figure 12 compares an image of a Pt trimer on a γ-alumina surface obtained with the uncorrected 300 kV STEM[32] to a

simulated image for a 0.5 Å probe, in which the Pt sites can be seen directly with respect to the different sites in the alumina support. The experimental images of La shown above are beginning to reveal such a level of insight.

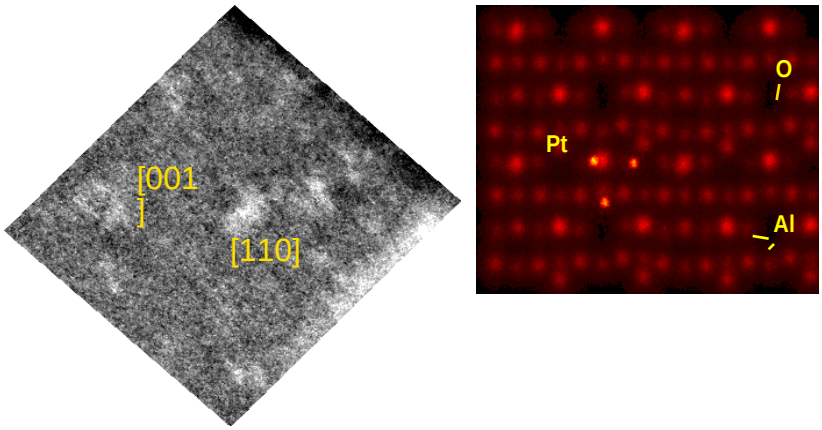

Fig. 12. (left) Z-contrast image at 1.3Å resolution showing Pt trimers and dimers on a γ-alumina support. (Right) Simulated image for a 0.5Å probe expected after correction of microscope aberrations.

Spectroscopy at the same spatial resolution will make possible determination of the electronic structure at *individual sites* surrounding such clusters, individual facets on a catalyst nanocrystal, even around single impurity or dopant atoms. In combination with theory, functionality could be understood at a fundamental level, luminescence efficiency of semiconductor nanocrystals, or how promoter atoms or poisons affect catalytic activity.

ACKNOWLEDGMENTS

We are grateful to the following for supply of samples: J. Santamaria and Z. Sefrioui for YBCO/LCMO superlattices, S. J. Rosenthal and J. McBride for nanocrystals, D. B. Geohegin and A. A. Puretzky for nanotubes, and J. Novak and M. Glazov for La-doped alumina. This research was supported by U.S. Department of Energy under Contract No. DE-AC05-00OR22725 managed by UT-Battelle, LLC, and by appointment to the ORNL Postdoctoral Research Program administered jointly by ORNL and ORISE. Research of M. Varela is performed as a Eugene P. Wigner Fellow and staff member at ORNL. Computation time was partially supported by the National Science Foundation under DMR990002N and DMR000004N and utilized the SGI Origin 2000 at the National Center for Supercomputing Applications, University of Illinois at Urbana-Champaign, and by the National Energy Research Scientific Computing Center, supported by the Office of Science of the U.S. Department of Energy under Contract No. DE-AC03-76SF00098.

REFERENCES

[1] S. J. Pennycook, G. Duscher, R. Buczko, M. Kim, N. D. Browning and S. T. Pantelides, in *Encyclopedia of Materials: Science and Technology*, Elsevier Science Ltd. 2313 (2001).

[2] X. Fan, E. C. Dickey, P. Eklund, K. A. Williams, L. Grigorian, R. S. Buczko, S. T. Pantelides and S. J. Pennycook, Phys. Rev. Lett. **84**, 4621 (2000).

[3] R. Buczko, S. J. Pennycook, and S. T. Pantelides, Phys. Rev. Lett. **84**, 943 (2000).

[4] M. Kim, G. Duscher, N.D. Browning, K. Sohlberg, S.T. Pantelides, and S.J. Pennycook, Phys. Rev. Lett. 86, 4056 (2001).

[5] E. M. James, N. D. Browning, A. W. Nicholls, M. Kawasaki, Y. Xin, and S. Stemmer, J. Elect. Micr. **47**, 561 (1998).
[6] M. Haider, S. Uhlemann, E. Schwan, H. Rose, B. Kabius and K Urban, Nature **392**, 768 (1998).
[7] O. L. Krivanek, N. Dellby and A. Lupini, Ultramicroscopy, **78**, 1 (1999).
[8] P. D. Nellist and S. J. Pennycook, Phys. Rev. Lett. **81**, 4156 (1998).
[9] S. J. Pennycook and P. D. Nellist In: D. G. Rickerby, U. Valdré and G. Valdré (eds.) *Impact of Electron and Scanning Probe Microscopy on Materials Research*, Kluwer Academic Publisers, The Netherlands, 161 (1999).
[10] P. D. Nellist and S. J. Pennycook, in P. W. Hawkes (ed.) *Advances in Imaging and Electron Physics*, Academic Press **113**, 148 (2000).
[11] S. J. Pennycook, in P. W. Hawkes (ed.) *Advances in Imaging and Electron Physics*, Academic Press **123**, 173 (2002).
[12] A. J. McGibbon, S. J. Pennycook, and J. E. Angelo, Science **269**, 519 (1995).
[13] M. M. McGibbon, N. D. Browning, M. F. Chisholm, A. J. McGibbon, and S. J. Pennycook, V. Ravikumar, and V. P. Dravid, Science **266**, 102 (1994).
[14] M. F. Chisholm and S. J. Pennycook. Mater. Res. Soc. Bull. **22**, 53 (1997)
[15] N. D. Browning, M. F. Chisholm, and S. J. Pennycook, Nature **366**, 143 (1993).
[16] G. Duscher, N. D. Browning, and S. J. Pennycook, Phys. Stat. Sol. (a) **166**, 327 (1998).
[17] M. F. Chisholm, A. Maiti, S. J. Pennycook, and S. T. Pantelides, Phys. Rev. Lett. **81**, 132 (1998).
[18] Y. Yan, M. F. Chisholm, G. Duscher, A. Maiti, S. J. Pennycook, and S. T. Pantelides, Phys. Rev. Lett. **81**, 3675 (1998).
[19] P. Hohenberg and W. Kohn, Phys. Rev. **136**, B864 (1964); W. Kohn and L.J. Sham, Phys. Rev. **140**, A1133 (1954).
[20] J. P. Perdew *et. al*., Phys. Rev. B **46**, 6671 (1992).
[21] D. Vanderbilt, Phys. Rev. **B41**, 7892 (1990).
[22] J. J. Shiang, A. V. Kadavanich, R. K. Grubbs and A. P. Alivisatos, J. Phys. Chem. **99**, 17417 (1995).
[23] H. J. Monkhorst and J. D. Pack, Phys. Rev. **B13**, 5188 (1976).
[24] P. M. Voyles, et al., *Nature*, **416**, 826 (2002).
[25] A. R. Lupini and S. J. Pennycook, Ultramicroscopy, in press.
[26] C. B. Murray, D. J. Norris, and M. G. Bawendi, J. Am. Chem. Soc. **115**, 8706 (1993).
[27] Andreas V. Kadavanich, Tadd C. Kippeny, Meg M. Erwin, Stephen J. Pennycook, and Sandra J. Rosenthal, J. Phys. Chem. **B105**, 361 (2001).
[28] L. W. Wang and A. Zunger, Phys. Rev. B **53**, 9579 (1996).
[29] L. G. Wang, S. J. Pennycook and S. T. Pantelides, Phys. Rev. Lett, **89**, 075506 (2002).
[30] X. Fan, R. Buczko, A. A. Puretzky, D. B. Geohegan, J. Y. Howe, S. T. Pantelides and S. J. Pennycook, Phys. Rev. Lett, in press (2002).
[31] S. J. Pennycook, B. Rafferty and P. D. Nellist, Microsc. Microanal. **6**, 34 (2000).
[32] P. D. Nellist, and S. J. Pennycook, Science **274**, 413 (1996).